Geoscience Frontiers 16 (2025) 102000

Contents lists available at ScienceDirect

Geoscience Frontiers

journal homepage: www.elsevier.com/locate/gsf

Research Paper

Polycyclic aromatic compounds in crude oil as proxies for Permian Tarim large igneous province activities

Rongzhen Qiao [a], Meijun Li [a,*], Donglin Zhang [a], Hong Xiao [a], Wenqiang Wang [b]

[a] National Key Laboratory of Petroleum Resources and Engineering, College of Geosciences, China University of Petroleum (Beijing), Beijing 102249, China
[b] School of Earth Sciences and Engineering, Xi'an Shiyou University, Xi'an, Shaanxi 710065, China

ARTICLE INFO

Article history:
Received 25 July 2024
Revised 12 November 2024
Accepted 25 December 2024
Available online 28 December 2024
Handling Editor: Richard Damian Nance

Keywords:
Large igneous province
Igneous intrusions
Hydrothermal
U-Pb dating
Polycyclic aromatic compounds

ABSTRACT

Large igneous provinces (LIPs), a critical area in Earth science, are closely related to paleoenvironmental evolution and biodiversity. The Permian Tarim large igneous province (TLIP) provides an ideal laboratory for correlational research. Previous reports show that the TLIP formed ~300–262 Ma. Based on igneous lithology and the upper limit of single magmatic activity (<5 Ma), the TLIP can be divided into five main magmatic episodes. Core logging, seismic sections, lithofacies observations, and in-situ calcite U-Pb dating indicate diabase intrusions and a hydrothermal upwelling event (~295.9–273 Ma) resulted from TLIP magmatic activity. The results indicate that polycyclic aromatic compounds (PACs) in oil are powerful proxies of magmatic intrusion and hydrothermal activity in the Permian TLIP. The existing diabase intrusion (EDI) samples show a higher concentration of high-molecular-weight (HMW) PACs (≥5-ring PACs) and greater combustion-derived PAC ratios. The distribution coupling between the diabase intrusion and PACs indicates that the HMW PACs are mainly derived from the cycloaddition reactions by the pyrogenic source (i.e., diabase intrusion). The conversion of phenanthrene (Phe), biphenyl (Bp), and dibenzothiophene (DBT) series compounds indicates that the oil is altered by hydrothermal activity. The hydrogenium and sulfur carried by the hydrothermal upwelling process promote the heteroatom incorporation of PACs. The cycloaddition and heteroatom incorporation reactions of PACs during the formation of LIPs offer a new perspective for evaluating their impact. PACs serve as effective proxies for LIPs and may also contribute to biological crises associated with LIPs.

1. Introduction

Over the past few decades, large igneous provinces (LIPs) have been a significant research focus in Earth science, representing intraplate tectonic igneous events throughout Earth's history (Bryan and Ferrari, 2013). At present, the best-recognized LIPs refer to the large-scale magmatic formation in the intraplate tectonic due to continuous or pulsating magmatism of short duration (Coffin and Eldholm, 1994; Bryan and Ernst, 2008). LIPs formation is typically closely associated with mantle plume activity (Morgan, 1971; Richards et al., 1989; Li and Powell, 2001; Cheng et al., 2018). Throughout geological history, extensive volcanic activity in LIPs has released significant amounts of cinder, toxic gases, and greenhouse gases (Svensen et al., 2004; Yang et al., 2020). These have a direct impact on the global climate and biodiversity (Wignall, 2001; Burgess et al., 2015). Additionally, investigations into LIPs are significant for understanding the formation of mineral resources (such as vanadium titanomagnetite, copper-nickel sulfide deposits, and other rare metal minerals) and their impact on petroleum systems (Hitzman et al., 1992; Pollard, 2006; Aarnes et al., 2010; Spacapan et al., 2018).

The Permian period (299–251 Ma) experienced relatively high volcanic activity in geological history. During this period, there were at least four large-scale flood basalt eruptions: the Tarim LIP (TLIP; ~300–262 Ma), the Himalayan magmatic province (HMP; ~290 Ma), the Emeishan LIP (ELIP; ~260 Ma), and the Siberian Traps (ST; ~252 Ma) (Supplementary Data Fig. S1; Sobolev et al., 2011; Shellnutt, 2014; Chen and Xu, 2019). Previous studies have shown that Permian LIPs contain significant petroleum resources in Paleozoic and Proterozoic reservoirs (Frolov et al., 2015; Feng et al., 2022; Xu et al., 2024). Magma and hydrothermal fluids migrate vertically and laterally along faults and unconformities (Langhorne, 2006; Cartwright, 2007). The flow of magma and hydrothermal fluids through the petroleum system accelerates hydrocarbon generation in source rocks (Othmana et al., 2001;

* Corresponding author.
E-mail address: meijunli@cup.edu.cn (M. Li).

https://doi.org/10.1016/j.gsf.2024.102000

Monreal et al., 2009), facilitates petroleum migration and accumulation (Schofield et al., 2015), enhances reservoir capacity (Duffy et al., 2021), induces large-scale oil cracking (Yang et al., 2022), and increases formation closure (Chukwuma et al., 2023). During this process, amounts of greenhouse gases (e.g., CH_4, CO_2) and toxic gases (e.g., H_2S) produced by petroleum pyrolysis, triggered by magmatic and hydrothermal activities, appear to be a crucial mechanism leading to global warming and biological extinction (Knoll and Grotzinger, 1996; Chen et al., 2022; Yang et al., 2022). However, the process produces more than just greenhouse and toxic gases. It also involves various reactions between different organic compounds, particularly the cycloaddition and heteroatom incorporation reactions of polycyclic aromatic compounds (PACs), which warrant significant attention (Xu et al., 2022). The abundance and distribution of combustion-derived PACs can effectively record thermal anomaly events in geological history (Fox et al., 2022; Jiao et al., 2023). PACs, persistent pollutants with extensive biological toxicity, are generally highly toxic, carcinogenic, teratogenic, mutagenic, and immunotoxic to various life forms (Lovelock et al., 1962; Peterson, 2003). The conversion of PACs from LIPs seems to need more attention.

The Tarim Basin, a typical LIP in China, contains abundant petroleum resources, particularly liquid hydrocarbons, within its Proterozoic and Paleozoic carbonate reservoirs (Zhu and Zhang, 2022; Zhang et al., 2024). This offers an excellent opportunity to investigate the impact of LIPs on organic fluid evolution. The diabase intrusion area of the Upper Ordovician in the Shunbei oilfield was delineated using core logging and seismic data. Core observation, in-situ calcite U-Pb dating, and organic geochemistry were employed to thoroughly evaluate the impact of LIP formations on PACs in organic fluids. This study offers a novel perspective on the influence of LIPs.

2. Geological setting

The Tarim Basin, located in northwest China, is bordered by the Kunlun, Tianshan, and Altyn orogenic belts, covering an area of 5.6×10^5 km^2 (Fig. 1a). It is the largest petroleum basin in China, composed of the Palaeozoic craton and Meso-Cenozoic foreland basins. From north to south, the Tarim Basin is generally divided into seven tectonic units: the Kuqa Depression, the Tabei Uplift, the Northern Depression, the Central Uplift, the Southwestern Depression, the Southern Uplift, and the Southeast Depression (Fig. 1a).

The Tarim Plate, hosting the Tarim Basin, is among the world's oldest cratons. The crystalline rock system formed in four primary stages: the Archean trondhjemite-tonalite-granodiorite evolution stage (2.8–2.5 Ga), the mid-late Paleoproterozoic A-type granite and basic dike swarm stage (2.0–1.8 Ga), the late Mesoproterozoic to late Neoproterozoic development of giant granite, basic dike swarms, ultramafic, and mafic rocks (1.0–0.9 Ga, 830–740 Ma, 650–630 Ma), and the Permian LIPs stage (300–262 Ma), characterized by flood basalts, basic dike swarms, granite, ultramafic, and mafic rock development (Zhang et al., 2013; Lu et al., 2023).

The Permian TLIP is the largest and most influential intra-plate magmatic event in the geological history of the region (Zhu and Zhang, 2022). It is widely distributed across the central and western parts of the Tarim Basin (Fig. 1a). Most of the igneous rocks are not completely exposed under the cover of the Taklimakan Desert. The primary types of igneous rocks are flood basalt and layered basic-ultrabasic intrusive rocks, followed by lamprophyres, diamondiferous kimberlites, alkaline igneous complexes, rhyolites, bimodal dyke swarms, and pyroclastic rocks (Zhu and Zhang, 2022). In recent years, petroleum drilling and geophysical prospecting have revealed that the coverage area of the TLIP exceeds 0.25×10^5 km^2 and the total volume of magma exceeds 0.15×10^5 km^2 (Fig. 1a; Xu et al., 2014).

3. Samples and methods

3.1. Samples

The samples for this study were obtained from petroleum wells in the Tabei and Shunbei oilfields (Fig. 1). A total of thirteen rock core and thirty-eight oil samples were collected from depths between 7,345 m and 9,145 m below the surface. Detailed sampling locations and types are shown in Fig. 1 and Supplementary Data Table S1. Additionally, the oil samples were collected directly from the wellhead. To prevent the loss of oil components, the samples were refrigerated during transportation to the China University of Petroleum (Beijing).

3.2. Analysis of aromatics in rocks and oils

After crushing the rock core sample, approximately 100 g of it was weighed, and the soluble organic matter was extracted using a Soxhlet apparatus. The powder samples were extracted with 300 mL of dichloromethane for 72 h and concentrated using a rotary evaporator.

Column chromatography was utilized to separate the extracts and oils. The sample was separated into asphaltenes, saturates, aromatics, and resins using elution solvents including petroleum ether, petroleum ether with dichloromethane (2:1, v/v), and dichloromethane with methanol (9:1, v/v).

Analysis of the aromatic fraction was conducted using gas chromatography-mass spectrometry (GC–MS) employing an Agilent 7890 GC/5975i MS system. The GC instrument was equipped with an HP-PONA column (internal diameter: 60 m × 0.25 mm, film thickness: 0.25 μm). For detailed temperature and testing program information, please refer to Qiao et al. (2024a). The quantification of aromatic fractions was conducted using known concentrations of d8-dibenzothiophene as internal standards.

3.3. Analysis of diamondoids and thiadiamondoids

Organic sulfur compounds (OSCs) were separated using a silver chromatography column. The preparation process included dissolving $AgNO_3$ in distilled water and impregnating 200-mesh silica gel, followed by activation at 105 °C for 4 h. The chromatography column was initially filled with $AgNO_3$-impregnated silica gel, followed by ordinary silica gel in a 3:2 ratio. The chromatography column was moistened with *n*-hexane, and the sample was dissolved by adding a few drops of *n*-hexane. Subsequently, the sample was loaded onto a chromatography column impregnated with $AgNO_3$. The saturates, aromatics, and OSCs were successively separated using *n*-hexane, dichloromethane, and acetone.

Analysis of the whole and OSC fractions was conducted using GC–MS employing an Agilent 7890 GC/5975i MS system. The GC instrument was equipped with an HP-PONA column (internal diameter: 60 m × 0.25 mm, film thickness: 0.25 μm). The analytical procedure began with heating the gas chromatograph to 60 °C and keeping for 2 min, followed by a ramp to 310 °C at a rate of 3 °C/min, with a subsequent keep for 5 min. The quantification of diamondoids and thiadiamondoids was conducted using known concentrations of d_{16}-Adamantan as internal standards.

3.4. Optical observation

Calcite vein samples from the Ordovician reservoir drilling cores in the Shunbei oilfield were collected for thin-section preparation.

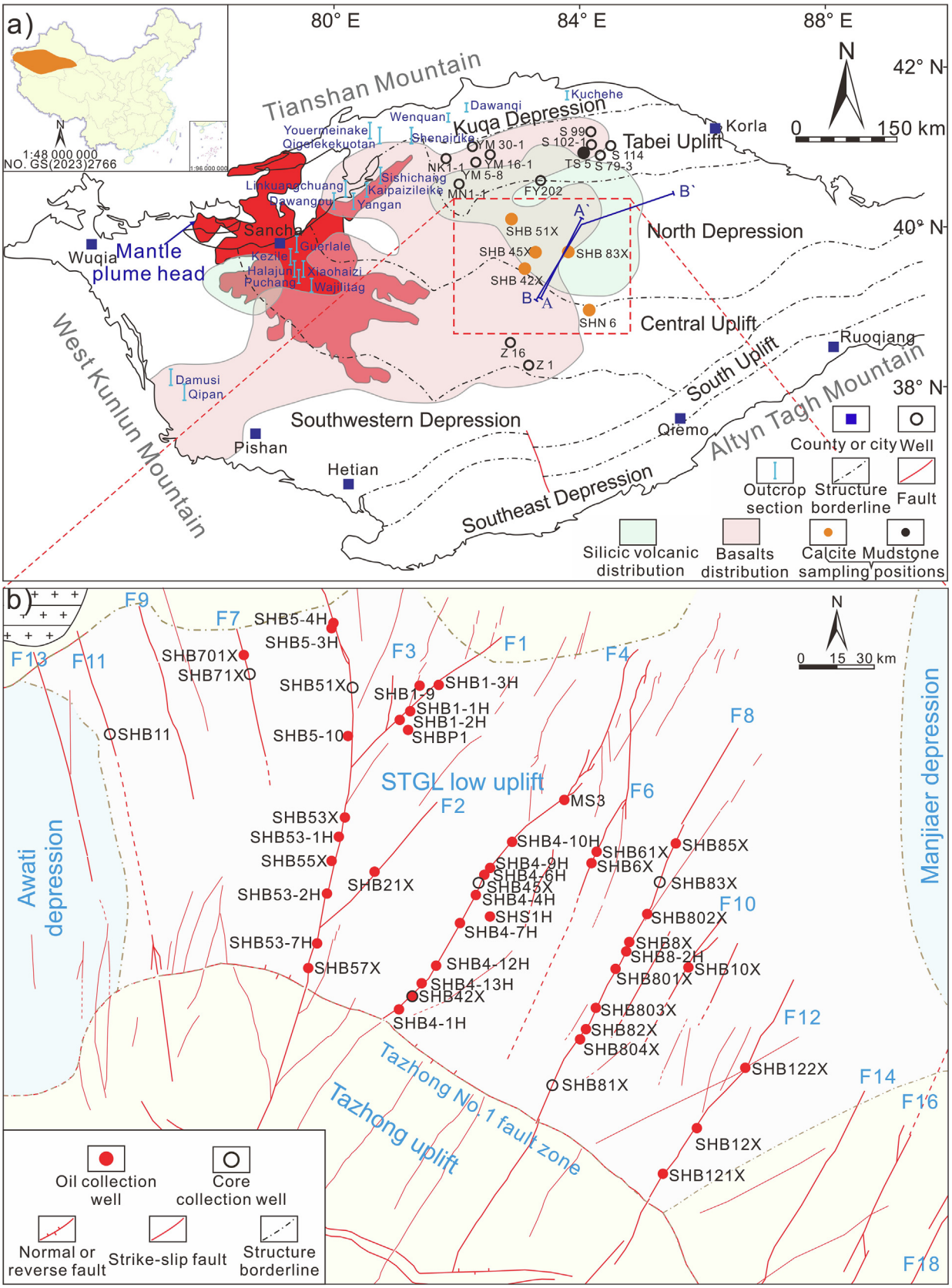

Fig. 1. (a) Tectonic sketch map of the Tarim Basin, with distributions of basalts and silicic volcanics in the Permian TLIP (revised after Liu et al., 2019), location and geometry of the mantle plume head (refer to Xu et al., 2020), and locations of petroleum wells and outcrops. (b) Tectonic sketch map of the Shunbei oilfield, with locations of the sampling petroleum wells. STGL low uplift: Shuntuoguole low uplift, Lines A–A‘ and B–B‘ represent the profiles shown in Fig. 2.

The samples were polished on both sides to a thickness of approximately 0.03 mm. Transmitted light, reflected light, and cathodoluminescence were observed using a Leica DM4500P polarizing microscope. The stages of calcite vein development are identified based on petrographic characteristics.

3.5. Calcite U–Pb dating

Samples for U-Pb dating are cut, cleaned, and made into targets approximately 1.5 cm thick. After polishing, the samples were washed in an ultrasonic bath for 30 min using a washing solution. Subsequently, the sample underwent three rounds of cleaning with deionized water and was dried on a hot plate at 40 °C to eliminate any surface contamination. The RESOlution SE laser and Thermo iCap-RQ quadrupole ICPMS were utilized for sample analysis. The calcite standard AHX-1B, with a measured age of 207.2 ± 2.0 Ma, was employed for further calibration of the $^{238}U/^{206}Pb$ ratio. The raw data underwent processing using the software Iolite v3.6 to obtain the corresponding isotope ratios. Subsequently, the concordia diagram and age calculation were performed using the software Isoplot 3.0. For detailed testing processes and standard sample information, please refer to Shen et al. (2019).

4. Results

4.1. Identification and distribution of igneous intrusions

Core logging reveals widely developed igneous intrusions of varying thickness in the Upper Ordovician strata of the Shunbei oilfield, predominantly composed of diabase (Fig. 2a and b). Seismic sections indicate that the diabase intrusions exhibit high-amplitude reflection characteristics and are roughly parallel to the sedimentary strata (Fig. 2c).

In the Shunbei oilfield, magma migrates upward along faults from the deep basin. Seismic reflections at the magma channel are characterized by chaotic and high-amplitude reflections (Supplementary Data Fig. S2a). After reaching the Upper Ordovician bottom (seismic interface as T_7^4), the magma began to flow laterally, forming diabase intrusions. The lateral continuity of these high-amplitude reflections is poor, often forming inclined dikes at both ends. Spatially, these intrusions exhibit saucer-shaped morphologies, concentrated between the T_7^4 and T_7^0 interfaces (Supplementary Data Fig. S2a). Additionally, the strata above the saucer-shaped sills tend to uplift due to the influence of diabase intrusions (Supplementary Data Fig. S2b).

Seismic section analysis reveals diabase intrusions in the F1, F5, F4, and F8 faults within the study area (Supplementary Data Fig. S2). No saucer-shaped intrusion is observed in the F12 fault (Supplementary Data Fig. S2f). Additionally, 3D seismic data further characterizes the diabase intrusion between the T_7^4 and T_7^0 interfaces in the Shunbei oilfield. According to the characterization results, the distribution range of diabase intrusion is described on the plane. The planar distribution of diabase intrusions and strike-slip fault zones indicates that intrusions are scattered between F13 and F10 faults (Supplementary Data Fig. S2g). The planar distribution of diabase intrusions in the Shunbei oilfield aligns with that of flood basalts and silicic volcanics in the Permian TLIP (Fig. 1a and Supplementary Data Fig. S2g).

4.2. Petrography

Drilling core observations showed prevalent yellow siliceous and hydrothermal alterations in the core of well SHB82X

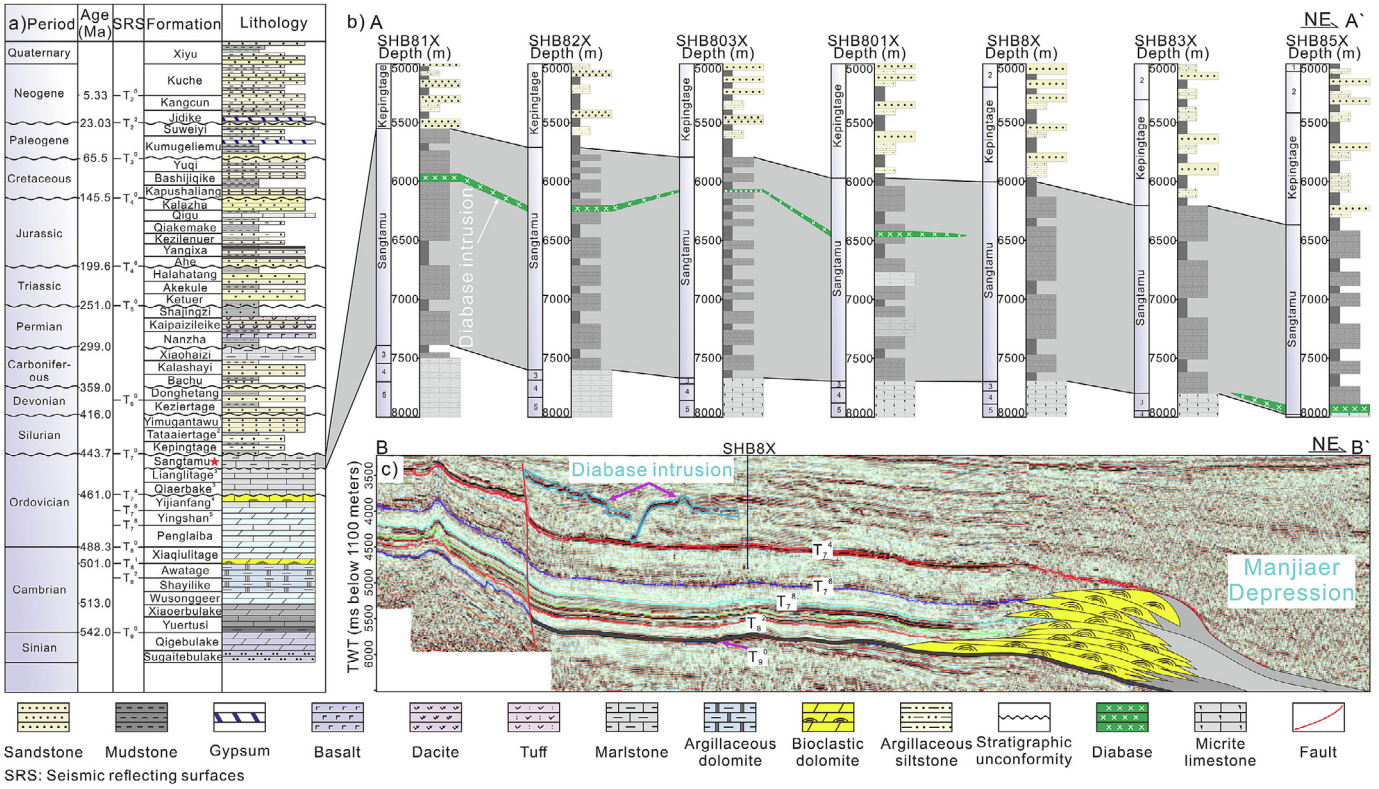

Fig. 2. (a) Generalized stratigraphy columns of the Shunbei oilfield, Tarim Basin. (b) Silurian-Ordovician well-tie profile in the No. 8 fault zone of Shunbei oilfield, Tarim Basin (Wells SHB81X, SHB82X, SHB803X, SHB801X, SHB8X, SHB83X, and SHB85X; see Fig. 1a for location). (c) Typical seismic section through SHB8X well in the Tarim Basin (see Fig. 1a for location).

(Supplementary Data Fig. S3a and b). Yellow siliceous and hydrothermal fluids were infiltrated along the fractures and were accompanied by pore development (Supplementary Data Fig. S3a and b). Microscopic and cathodoluminescence analyses revealed two phases of calcite cement in the Middle and Lower Ordovician carbonate reservoirs of the Shunbei oilfield (Supplementary Data Fig. S3c and d). The cathodoluminescence of calcite cement in the first (C1) and second (C2) phases shows dim brownish-yellow and luminous yellow hues, respectively (Supplementary Data Fig. S3c and d). The C2 calcite cement predominantly developed along high-angle structural fractures (Supplementary Data Fig. S3e). The SHB42X cores exhibited bitumen filling and semi-filling in the C2 calcite cement (Supplementary Data Fig. S3e).

4.3. Calcite U–Pb dating results

Seven calcite veins and cements from Ordovician reservoirs in the Shunbei oilfield were chosen for U-Pb dating. The samples exhibited low common lead concentrations and high $^{238}U/^{206}Pb$ ratios. The high $^{238}U/^{206}Pb$ ratios (>7) were crucial for the success of the in-situ calcite U-Pb dating. In addition, the error coefficient of in-situ calcite U-Pb dating is below 8.5%, and the MSWD values range from 1.9 to 2.9, indicating reliable dating results.

The results show that the formation ages of the C1 calcite cement in the Ordovician reservoir in the Shunbei oilfield are 465.3 ± 7.8 Ma (N = 32; MSWD = 1.9), 434.0 ± 14.0 Ma (N = 56; MSWD = 2.9), 410.0 ± 24.0 Ma (N = 51; MSWD = 2.2), and 351.0 ± 30.0 Ma (N = 12; MSWD = 1.9), respectively (Supplementary Data Table S2). The formation ages of the C2 calcite cement are 295.9 ± 5.2 Ma (N = 27; MSWD = 2.9) and 273.0 ± 7.5 Ma (N = 37; MSWD = 1.3) (Supplementary Data Table S2).

4.4. Identification and distribution of polycyclic aromatic compounds

The total ion chromatography (TIC) of the aromatic components from the samples shows significant differences (Fig. 3). Among them, the TIC of aromatic components from the existing diabase intrusion (EDI) samples shows baseline humps (Fig. 3c1 and d1). GC–MS of the aromatic fractions detected > 3-ring PACs in addition to naphthalene (Nap), biphenyl (Bp), phenanthrene (Phe), and dibenzothiophene (DBT) and their alkylation derivatives (Fig. 3). Notably, compared with the no diabase intrusion (NDI) samples, the EDI samples contain higher abundances of 6-ring and 7-ring PACs (Fig. 3). Compared to oils, cores experience varying degrees of light-molecular-weight aromatic hydrocarbon loss during preservation and Soxhlet extraction. Consequently, core analysis primarily focuses on > 4-ring PACs. In addition, the compound names, abbreviations, molecular formulas, and $M^+(m/z)$ information of the PACs involved in this study are recorded in detail in Supplementary Data Table S3. Supplementary Data Fig. S4 provides the mass spectrum of the PACs involved in this study.

4.5. Thiadiamondoid compounds

GC–MS analysis of the thiadiamondoids revealed that the oils did not contain thiadiamondoids with more than three cages. In addition, only thiaadamantane and thiadiamantane series compounds were detected in most oils, while thiatriamantane series compounds were detected in a small number of oils (Supplementary Data Fig. S5). Moreover, quantitative analysis showed that the thiaadamantanes concentration in oils ranged from 0.09 to 177.02 μg/g, with an average value of 13.98 μg/g (Supplementary Data Table S4).

5. Discussion

5.1. Magmatic activity and age of Permian TLIP

In the past 30 years, numerous geochronology studies have used various analytical methods to investigate different igneous types in the TLIP (Li et al., 2007; Dong et al., 2013; Liu et al., 2019, 2023). A summary of 83 sets of reliable dating data reveals that the formation time of the TLIP ranges from 300.8 Ma to 263.1 Ma (Supplementary Data Fig. S6 and Table S2). The total duration of the TLIP exceeds 37 Ma, which differs significantly from that of the ELIP (~260 Ma) and the ST (~252 Ma) (Supplementary Data Fig. S6, Prasanth et al., 2022). The TLIP can be further divided into five main magmatic episodes based on lithofacies, dating data,

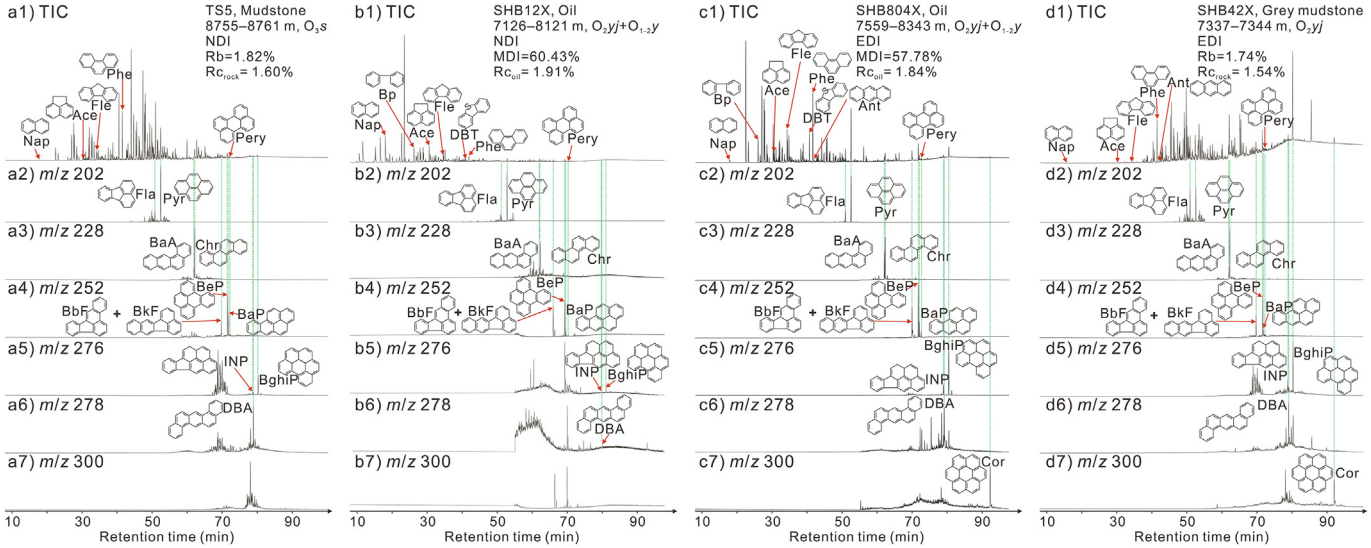

Fig. 3. Total ion chromatograms of aromatic hydrocarbon fractions and mass chromatograms of polycyclic aromatic hydrocarbons (m/z 202, m/z 228, m/z 252, m/z 276, m/z 278, and m/z 300) for representative drill hole cores (TS5 and SHB42X) and oils (SHB12X and SHB804X) in the Cambrian-Ordovician from the Shunbei and Tabei oilfields. Rc_{rock}: The equivalent vitrinite reflectance of bitumen (calculated according to the bitumen reflectance, Rb), Rc_{rock} = 0.346+ 0.688Rb (Rb<2.0%, Jacob, 1989); MDI: methyldiamantane index; MDI = 4-MD/(1-MD+3-MD+4-MD); MD: methyldiamantane; Rc_{oil}: Rc_{oil} = 0.4389+0.0243MDI (Chen et al., 1996); EDI: Exist diabase intrusion; NDI: No diabase intrusion. For abbreviations of PACs, see Supplementary Data Table S3.

and the upper limit of single magmatic duration (<5 Ma) (Bryan and Ernst, 2008).

The magmatic activity in the TLIP began ~ 300 Ma (Supplementary Data Fig. S6). The initial lithology is kimberlite, which is confined to the Wajilitag area (Fig. 1a; Lu et al., 2023). From ~ 294 Ma to ~ 268 Ma, there were three episodes of flood basalt eruptions. The effusive rocks are mainly basalt and rhyolite, with peak ages at ~ 290 Ma, ~280 Ma, and ~ 272 Ma (Supplementary Data Fig. S6a). During these three main magmatic eruption episodes, the peak ages of effusive and intrusive rocks show some differences (Supplementary Data Fig. S6b). However, the difference between the peak ages of effusive and intrusive rocks within each episode is < 5 Ma (Supplementary Data Fig. S6b). The alternating occurrence of igneous and clastic rocks in the Permian strata supports the conclusion of multiple episodes of eruptions (Supplementary Data Fig. S6a; Lu et al., 2023). After ~ 266 Ma, magmatic activity in the TLIP entered its late stage. At this time, local diabase intrusions predominated (Supplementary Data Fig. S6a). Notably, the starting and ending igneous types in the TLIP are intrusive rocks (Supplementary Data Fig. S6b). This observation is also consistent with magma dynamics (Cashman et al., 2017). Furthermore, long-term, multiple episodes of magmatic activity and limited magma volume result in a low eruption rate in the TLIP (Liu et al., 2019).

5.2. TLIP as a trigger mechanism for hydrothermal activity

The relationship between igneous eruptions in LIPs and hydrothermal circulation in deep reservoirs has garnered significant interest (Dong et al., 2013; Su et al., 2024). Primarily, two phases of calcite cement are developed in the Ordovician reservoirs of the Shunbei oilfield (Fig. 4). The formation of C2 calcite cement occurred between 295.9 ± 5.2 Ma and 273 ± 7.5 Ma, which is in the interval of the Permian TLIP (Fig. 4 and Supplementary Data Table S2). Moreover, a temporal comparison of C2 calcite cement formation and diabase intrusion in the Tarim Basin shows significant overlap (Fig. 4). This indicates a potential internal relationship between diabase intrusion and C2 calcite cement formation in the Shunbei oilfield.

Previous studies indicate that a negative $\delta^{18}O$ excursion and the rare earth element distribution in C2 calcite cement exhibit a clear positive Eu anomaly (Li et al., 2023). This suggests that the formation of C2 calcite cement is primarily influenced by deep hydrothermal fluids. The regional thermal anomaly induced by the Permian TLIP provided advantageous conditions for sustained hydrothermal activity (Li et al., 2022). A distinct yellow siliceous infilling was observed in the cores, indicating that the sandstone strata of the Sinian Sugaitbulak Formation (Z_1s) served as feeder aquifers for long-distance hydrothermal fluid migration (Supplementary Data Fig. S3 a and b; Dong et al., 2017). Permian fault reactivation provided a channel for magma and hydrothermal upwelling (Davies et al., 2006; He et al., 2019). Furthermore, the $^{87}Sr/^{86}Sr$ values in C2 calcite cement range from 0.709634 to 0.711004 (Li et al., 2023). These values are significantly higher than those of surrounding rock and normal seawater from the Middle to Late Cambrian and closely match the global average derived from crustal sources (Palmer and Elderfield, 1985; Cai et al., 2008). This indicates that the hydrothermal fluid was not only sourced from the deep sandstone feeder aquifer but was also contributed by crustal material.

5.3. Cycloaddition reactions of PACs indicate magma intrusion

The distribution of PACs is influenced by the source of organic matter, diagenesis, and metamorphism, as well as by thermal anomaly events (e.g., wildfires, magmatic activity, and hydrothermal activity) throughout geological history (Yunker et al., 2002; Hudspith et al., 2012; Xu et al., 2021). The high-molecular-weight (HMW) PACs (≥5-ring PACs) are typically formed under high-temperature conditions (Xu et al., 2021; Qiao et al., 2024a). Early studies suggest that the first oil charging occurred in the late Caledonian period in the Shunbei oilfields (Qiao et al., 2024a). And the Re-Os isotopic data of bitumen from the Ordovician Yijianfang Formation in well SHB1-3H indicates an isochron age of 399 ± 12 Ma (Wu et al., 2021). Based on the time sequence, the Permian TLIP may have influenced the Ordovician reservoir oils (Fig. 4). The EDI samples contain a higher abundance of HMW PACs, particularly coronene (Fig. 3). This suggests an intrinsic genetic relationship between the distribution of PACs and diabase intrusions. Furthermore, the relative distribution of combustion-derived PACs is often used to identify their source (petrogenic or pyrogenic) (Simoneit and Fetzer, 1996). Previous studies have demonstrated that thermal anomaly events often increase the combustion-derived PAC ratios in sediments and oils, including fluoranthene (Fla)/(Fla + pyrene (Pyr)), indeno[1,2,3-cd] pyrene (INP)/(INP + benzo[ghi]perylene (BghiP)), and benzo[a]anthracene (BaA)/(BaA + chrysene (Chy)) (Yunker et al., 2002). Cross-plots of combustion-derived PAC ratios indicate significant differences between EDI and NDI samples (Fig. 5). NDI samples are located in zones associated with petrogenic origins, while EDI samples are primarily found in mixed zones associated with combustion (Fig. 5). This suggests that the increased combustion-derived PAC ratios result from diabase intrusion in the Permian TLIP. Additionally, when magma flows through petroleum systems, the combustion of oil is unlikely due to the lack of oxygen. Instead, the magma causes thermal alteration through baking rather than combustion. Therefore, although the combustion-derived PAC ratios in the study area have increased significantly, most are located in the mixed zones rather than in the petroleum combustion zones.

Early studies have shown that combustion-derived PACs with 3- and 4-rings are typically produced by moderate- to low-temperature combustion (ranging from 300 ℃ to 600 ℃) (Karp et al., 2020). As charring temperature increases, the abundance of HMW PACs rises gradually (Wiedemeier et al., 2015). Therefore, this study investigated the impact of diabase intrusion by analyzing the relative abundance of 6- and 7-ring PACs in the samples. Ternary analysis of BghiP, INP, and Cor shows an increase in the relative abundance of INP and Cor from NDI to EDI samples (Fig. 6). Combined with the distribution range analysis of diabase intrusion, it is found that the content of INP and Cor in the EDI samples accounts for more than 25% of the ternary (BghiP, INP, and Cor) total content (Supplementary Data Fig. S7 and Table S5). This indicates that the thermal anomalies from diabase intrusion caused an increase in the relative abundance of INP and Cor in samples (Simoneit and Fetzer, 1996; Qiao et al., 2024a). Previous studies indicate that the influence range of intrusive is typically 1–2 times its thickness (Othman et al., 2001). For the Tarim Basin, in addition to the distribution of intrusions, the thermal influence of magma upwelling along strike-slip faults on reservoirs should also be considered. However, limitations in exploration and the unknown resource quantity in the basin pose significant challenges to the detailed evaluation of the environmental impact of PACs formed in the Permian TLIP.

5.4. Heteroatom incorporation of PACs indicates hydrothermal activity

During hydrothermal activity, the addition of hydrogenium, sulfur, and metal ions typically promotes the conversion of organic compounds (Simoneit and Fetzer, 1996; McCollom et al., 2001; Xu et al., 2022; Qiao et al., 2024b). The concentration of dibenzothiophene series (DBTs) in the oil of the Shunbei oilfield ranges from

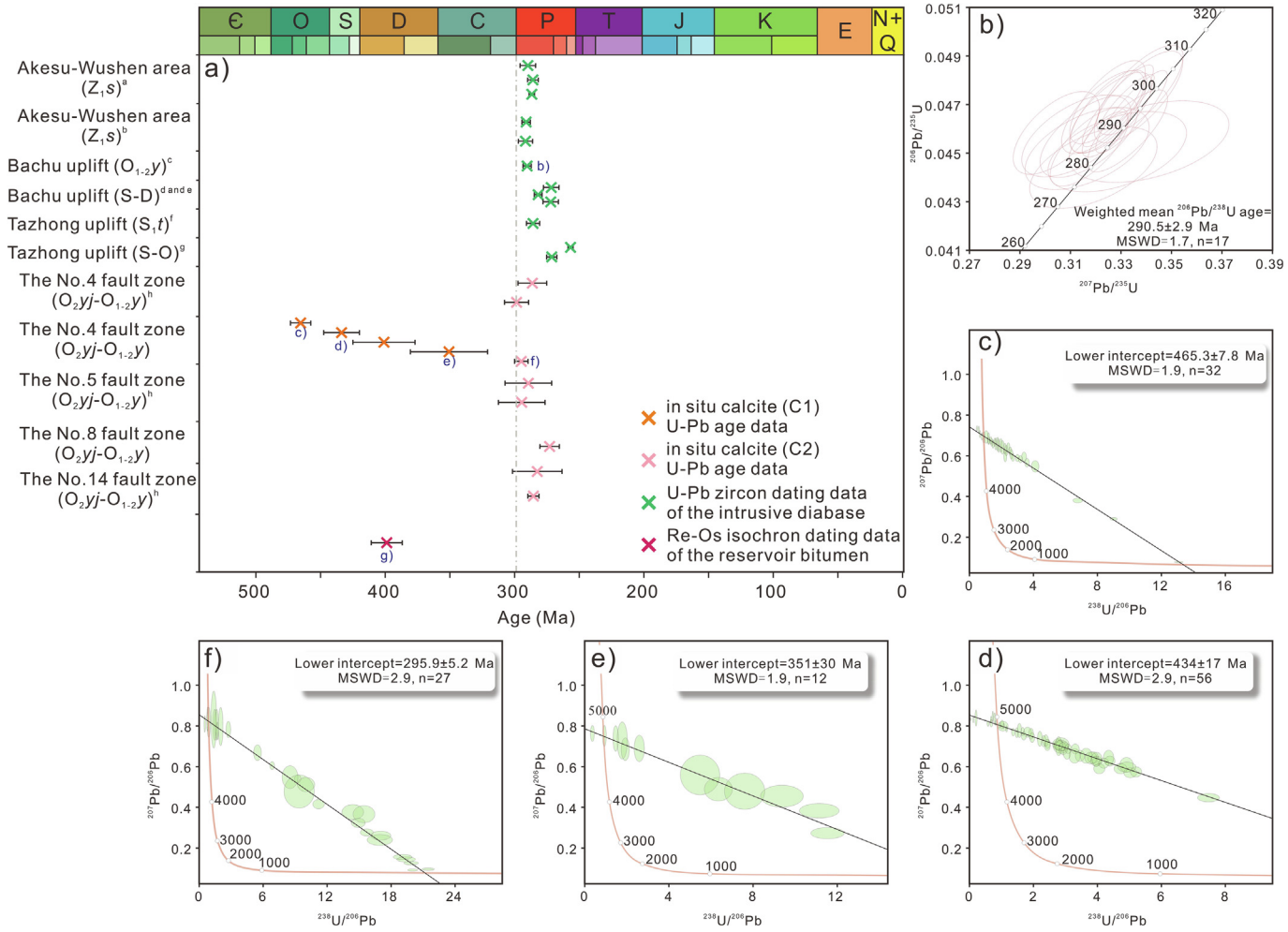

Fig. 4. Diabase intrusion zircon and in situ calcite U-Pb dating ages from the Ordovician in the Tarim Basin (Fig. 4b is from Dong et al., 2013). [a] Cheng et al., 2022; [b] Wu et al., 2020; [c] Dong et al., 2013; [d] Zhang et al., 2009; [e] Li et al., 2007; [f] Li et al., 2017; [g] Zhang et al., 2010b; [h] Li et al., 2023.

2.44 to 1711.51 μg/g, which shows significant variation (Supplementary Data Table S4). Previous studies indicate that in addition to sulfur incorporation during deposition and diagenetic sulfurization at low temperatures, DBTs can also form through secondary processes like hydrothermal alteration and TSR (Cai et al., 2009a; Xu et al., 2022; Wang et al., 2023).

Sulfur isotope analysis indicates that Cambrian source rocks primarily contribute to the Ordovician reservoirs in the Tarim Basin (Cai et al., 2009b, 2015). Furthermore, extensive drilling, outcrop, and sedimentary facies studies have confirmed that black mudstone of the Lower Cambrian Yuertusi Formation is the main source rock of the Ordovician petroleum system (Zhu et al., 2020; Qiao et al., 2024a). This suggests that lithology and sedimentary environment are not the primary factors affecting DBT series concentration differences in the study area. Thiaadamantane content indicates that only five wells in the southern part of F5 and F4 faults were affected by TSR (TAs > 20 μg/g) (Supplementary Data Fig. S8 and Table S4). Early studies suggested that TSR would lead to an increase in DBT series concentrations in oil (Orr, 1974; Cai et al., 2016, 2022). The correlation coefficient between DBT series and TAs concentrations in oil from the Shunbei oilfield is only 0.1606, which indicates that TSR may not significantly affect DBT series concentration (Supplementary Data Fig. S9). Previous studies have shown that the $\delta^{34}S$ values of DBT series in the SHB42X oil (TAs > 20 μg) range from 19.0‰ to 23.4‰ (Wang et al., 2024). These $\delta^{34}S$ values are similar to those of kerogen from Cambrian source rocks (14.0‰–21.6‰) (Cai et al., 2015), but they differ significantly from Cambrian anhydrite (26.8‰–34.1‰) and Ordovician anhydrite (26.0‰) (Cai et al., 2001; Cai et al., 2016). This comprehensive analysis suggests that TSR in the Ordovician reservoir is localized and limited and is not the primary factor behind the DBT series concentration differences observed in the Shunbei oilfield (Qiao et al., 2024b). Therefore, the impact of hydrothermal activities on DBT series concentrations in Ordovician oil of the study area needs re-evaluation.

Comparing the relative abundance of Phe, Bp, and DBT series compounds in oils reveals significant differences across different fault zones (Fig. 7a). Previous studies have shown low levels of Bp series compounds in oils unaffected by hydrothermal activity (Xu et al., 2022). Under hydrothermal influence, Phe series compounds can transform into Bp through ring-opening oxidation (Fig. 7a; Püttmann et al., 1989). When the Cambrian gypsum-salt layer exceeds 200 m, corresponding Ordovician oils exhibit higher DBTs concentrations (Fig. 7 and Supplementary Data Table S4). This is likely because hydrothermal fluid carries more sulfur as it flows through the gypsum-salt layer during upwelling. The addition of sulfur promotes the conversion of thermally unstable Bp series compounds to DBT series compounds (Fig. 7a; Xu et al., 2022). Similar patterns were observed in the ternary plots of 'Phe – Bp – DBT', '3-+1-methylphenanthrenes (MPhe) – 3-methylbiphenyl (MBp) – 4-methyldibenzothiophene (DBT)', and '2-MPhe – 4-MBp – DBT' (Fig. 7b, c, and d).

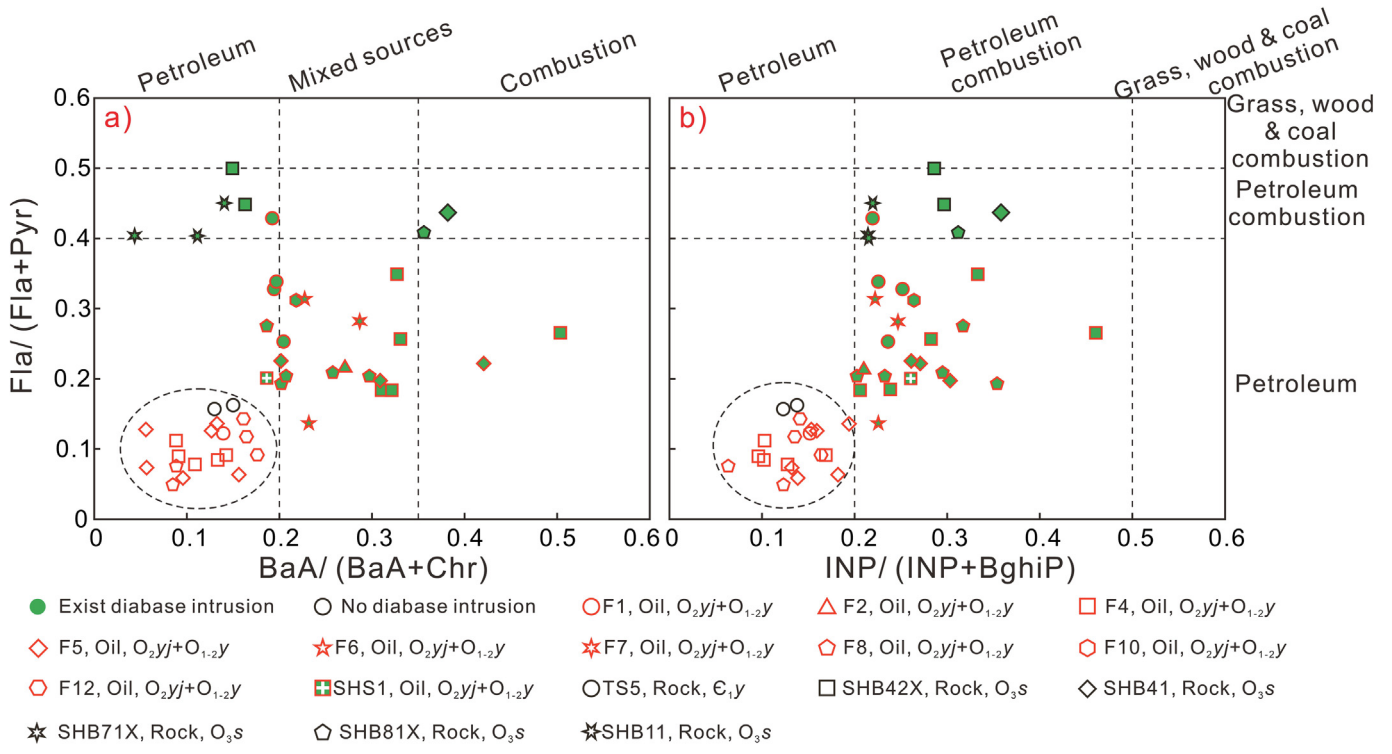

Fig. 5. Cross-plots indicating the origin of PACs. (a) Fla/(Fla+Pyr) vs. BaA/(BaA+Chr) (refer to Yunker et al., 2002); (b) Fla/(Fla+Pyr) vs. INP/(INP+BghiP) (refer to Yunker et al., 2002). Fla: Fluoranthene; Pyr: Pyrene; BaA: Benz[a]anthracene; Chr: Chrysene; INP: Indeno[1,2,3-cd]pyrene; BghiP: Benzo[g,h,i]perylene.

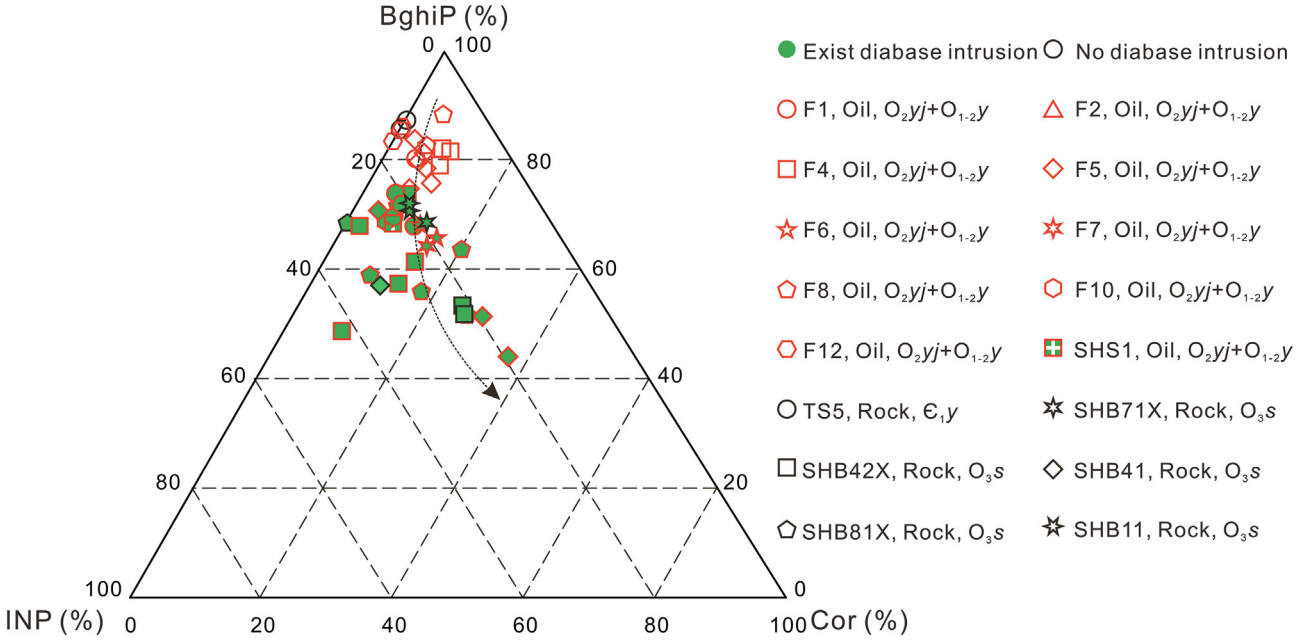

Fig. 6. Ternary diagrams showing the relative abundance of Benzo[g,h,i]perylene (BghiP), Indeno[1,2,3-cd]pyrene (INP), and Coronene (Cor) (refer to Qiao et al., 2024a).

The relative abundance of Phe, Bp, and DBT series compounds in oils indicates significant hydrothermal alteration in the Shunbei oilfield. The thickness of the Cambrian gypsum-salt layer influences the amount of sulfur carried by hydrothermal fluids, leading to differences in sulfur-containing PACs concentration in the oils.

5.5. PACs conversion and implications in the Permian TLIP

The Permian TLIP consists of multiple episodes of magmatic activity spanning > 37 Ma. At ~ 300 Ma, the metamorphic material at the base of the lithosphere partially melted due to mantle plume

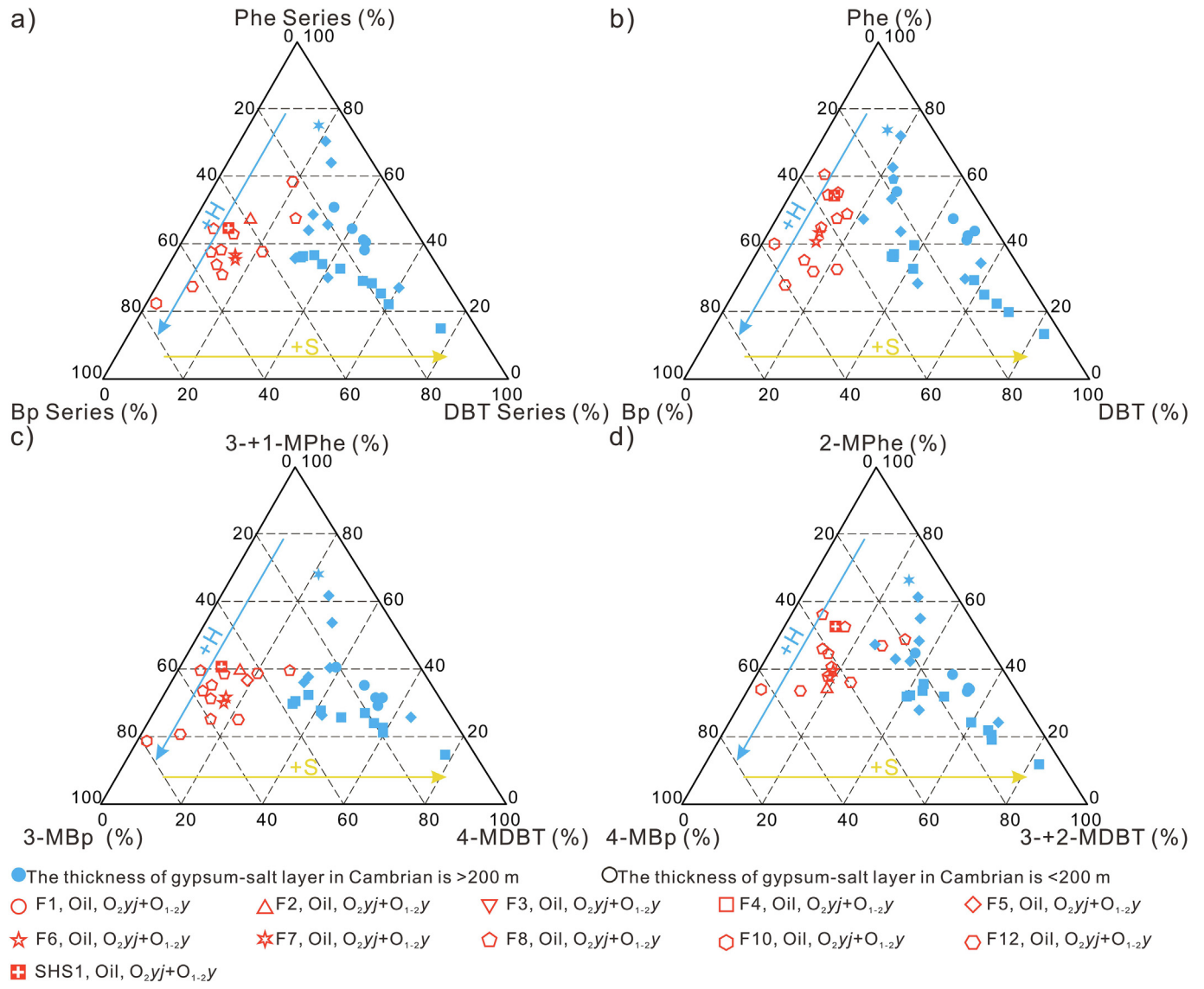

Fig. 7. Ternary diagrams showing the relative abundance of (a) phenanthrene (Phe) series, biphenyl (Bp) series, and dibenzothiophene (DBT) series, (b) Phe, Bp, and DBT, (c) 3- +1-methylphenanthrene (3-+1-MPhe), 3-methylbiphenyl (3-MBp), and 4-methyldibenzothiophene (4-MDBT), and (d) 2-methylphenanthrene (2-MPhe), 4-methylbiphenyl (4-MBp), and 3-+2-methyldibenzothiophene (3-+2-MDBT).

heating, initiating kimberlite intrusion in the Bachu area (Fig. 8a). This event marks the beginning of the Permian TLIP, though the initial intrusion was limited in scale and scope (Zhang et al., 2013).

Subsequently, around 294 Ma, continuous mantle plume heating initiated a large-scale flood basalt eruption episode in the TLIP. Between 294 Ma and 268 Ma, controlled by eruptive decompression and intermittent magmatic replenishment, this period can be divided into three episodes of flood basalt eruptions (Fig. 8b; Cashman et al., 2017). Following each large flood basalt eruption, the mantle plume upwelled along the magma channel, forming basic-ultrabasic intrusions. Following each large flood basalt eruption, the mantle plume upwelled along the magma channel, forming basic-ultrabasic intrusions. The oil is baked as the intrusion upwells through the petroleum system. Magmatic intrusion affected the cycloaddition reactions of PACs in oil (Fig. 8b1). This process directly leads to the detection of high concentrations of HMW PACs in light oils and condensates (Fig. 3). Simultaneously, continuous interaction between the mantle plume and lithosphere caused gradual lithospheric thinning. The remaining basalt in the lithospheric magma chamber underwent crystal differentiation to form rhyolite, which subsequently erupted to the surface (Fig. 8b; Wei et al., 2019). Additionally, prolonged mantle plume heating induced hydrothermal activity in the Tarim Basin. Under hydrothermal influence, calcite veins of hydrothermal origin formed in the Ordovician, along with widely distributed barite, fluorite, and chert (He et al., 2019). Furthermore, hydrothermal fluids facilitated extensive organic–inorganic interactions in the basin's deep organic fluids, leading to the conversion of Phe, Bp, and DBT series compounds (Fig. 8b2).

After ~ 268 Ma, following a large-scale flood basalt eruption, the Permian TLIP entered its late evolutionary stage (Fig. 8c). During this period, crustal melting and the formation of low-temperature rhyolite became increasingly difficult. However, localized dissolution occurred near the mantle plume head, forming a basic-ultrabasic intrusive with a depleted mantle (Fig. 8c; Zhang et al., 2010).

Considerable research strongly suggests that greenhouse gas and toxic gas emissions from the pyrolysis of paleo-oil reservoirs in the Permian LIPs may have been an important mechanism in the late Permian biocrisis (Knoll and Grotzinger, 1996; Chen

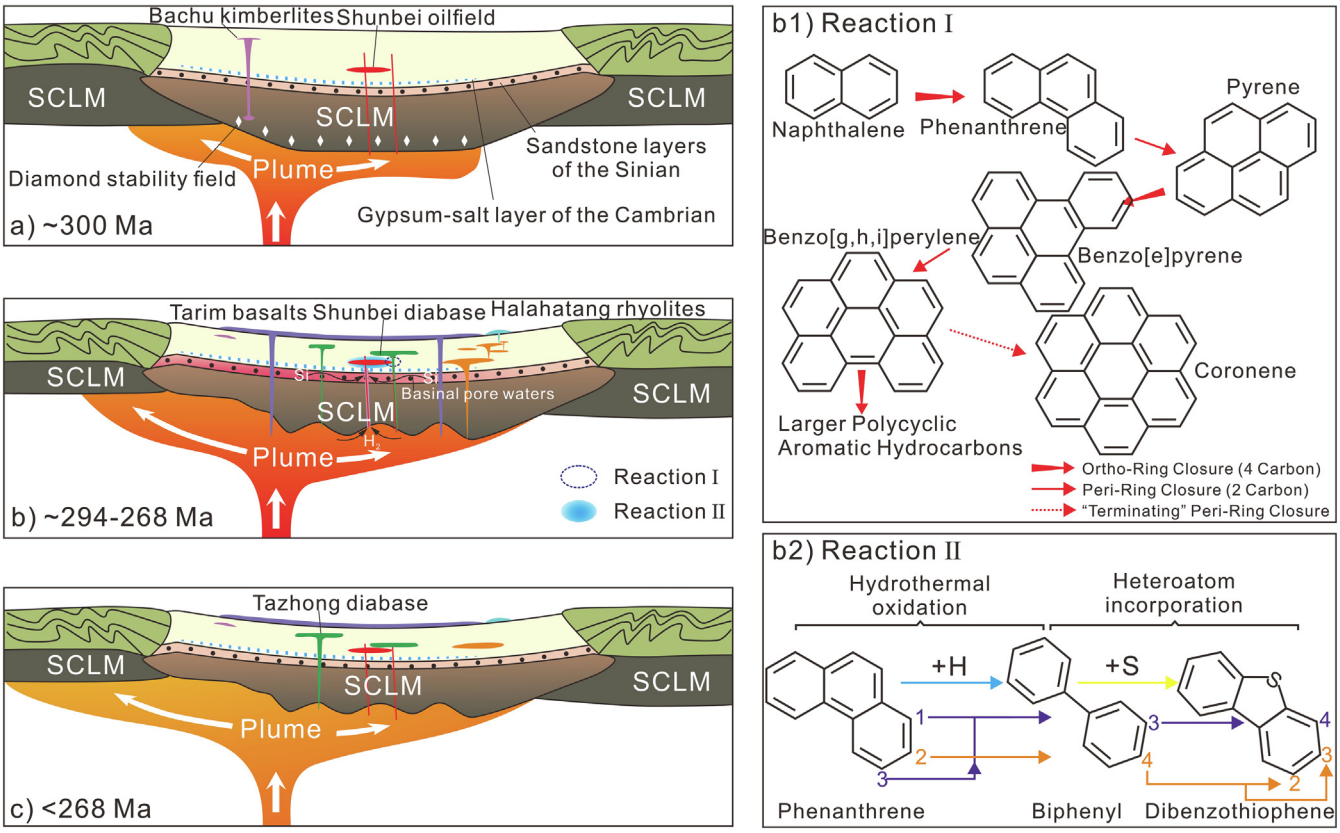

Fig. 8. Formation model of the Permian TLIP and conversion pathway of organic compounds. (a) At ~300 Ma, under the influence of mantle plumes, kimberlite begins to intrusion; (b) at ~294–268 Ma, under the continuous heating of the mantle plume, the magmatic activity becomes stronger, and the effusive and intrusive rocks begin to erupt and invade on a large scale; (b1) the transformation pathway of the ring addition of PACs under the influence of igneous intrusions (refer to Simoneit et al., 1981); (b2) conceptional multiple reaction pathways of PACs under the influence of the hydrothermal activity (refer to Simoneit and Fetzer, 1996); (c) After ~268 Ma, the magmatic activity is gradually weakening, and a small amount of diabase intrusion is found in the central area of magmatic activity. STGL: Sub-continental lithospheric mantle.

et al., 2022; Yang et al., 2022). Significant amounts of liquid hydrocarbons are present in Paleozoic reservoirs in the Tarim Basin. During the formation of the Permian TLIP, extensive magmatic intrusions and hydrothermal activities promoted cycloaddition reactions and heteroatom incorporation of PACs. The increased concentration of HMW PACs and S-containing PACs may have contributed to late Permian biocrisis. Magma may have transported PACs to the surface during eruptions, which is lethal to most fauna on Earth (Lovelock et al., 1962; Peterson, 2003). Furthermore, tectonic uplifts during the Late Permian-Early Triassic and Paleogene exposed some paleo-oil reservoirs rich in HMW PACs and sulfur-containing PACs, which likely affected the environment (Dong et al., 2013).

6. Conclusions

The Permian TLIP (~300–262 Ma) consists of multiple episodes of magmatic activity spanning > 37 Ma. Based on igneous lithology and the upper limit of single magmatic activity (<5 Ma), the TLIP can be divided into five main magmatic episodes: ~300 Ma, ~290 Ma, ~280 Ma, ~272 Ma, and ~ 263 Ma.

Core logging and seismic sections show that a set of diabase intrusions was formed in the upper Ordovician sedimentary strata of the Shunbei oilfield during the Permian TLIP. Lithofacies observations and in-situ calcite U-Pb dating indicate that a period of hydrothermal upwelling events (~295.9–273 Ma) was formed due to the influence of magmatic activity in the Permian TLIP.

The mass chromatograms of PACs show that the EDI oils have a higher abundance of HMW PACs (≥5-ring PACs), especially coronene. The combustion-derived PAC ratios indicate that the EDI oil and the NDI oil have a clear distinction. This indicates that the HMW PACs in oil are mainly derived from the cycloaddition reactions caused by the diabase intrusion.

The conversion of Phe, Bp, and DBT series compounds indicates that the oil is altered by hydrothermal activity. The hydrogenium and sulfur carried by the hydrothermal upwelling process promote the heteroatom incorporation of PACs.

These results indicate that PACs can effectively record magmatic and hydrothermal activities within LIPs. The conversion of PACs leads to an increase in HMW and sulfur-containing PACs, which may be a crucial mechanism affecting biodiversity in the LIPs. This PAC conversion offers a novel perspective for further exploring the impact of LIPs.

CRediT authorship contribution statement

Rongzhen Qiao: Writing – review & editing, Writing – original draft, Methodology, Conceptualization. **Meijun Li:** Writing – review & editing, Visualization, Supervision. **Donglin Zhang:** Software, Investigation, Data curation. **Hong Xiao:** Validation, Resources. **Wenqiang Wang:** Investigation.

Declaration of competing interest

The authors declare that they have no known competing financial interests or personal relationships that could have appeared to influence the work reported in this paper.

Acknowledgements

This work was funded by the National Natural Science Foundation of China (Grant No. 42173054). The author expresses gratitude to the Associate Editors, R. Damian Nance, and the four anonymous reviewers for their valuable and constructive reviews, which have significantly enhanced the manuscript.

Appendix A. Supplementary data

Supplementary data to this article can be found online at https://doi.org/10.1016/j.gsf.2024.102000.

References

Aarnes, I., Svensen, H., Connolly, J.A.D., Podladchiko, Y.Y., 2010. How contact metamorphism can trigger global climate changes: Modeling gas generation around igneous sills in sedimentary basins. Geochim. Cosmochim. Acta 74 (25), 7179–7195. https://doi.org/10.1016/j.gca.2010.09.011.

Bryan, S.E., Ernst, R.E., 2008. Revised definition of large igneous provinces (LIPs). Earth-Sci. Rev. 86 (1–4), 175–202. https://doi.org/10.1016/j.earscirev.2007.08.008.

Bryan, S.E., Ferrari, L., 2013. Large igneous provinces and silicic large igneous provinces: Progress in our understanding over the last 25 years. GSA Bulletin 125 (7–8), 1053–1078. https://doi.org/10.1130/B30820.1.

Burgess, S.D., Bowring, S.A., Fleming, T.H., Elliot, D.H., 2015. High-precision geochronology links the Ferrar large igneous province with early-Jurassic ocean anoxia and biotic crisis. Earth Planet. Sci. Lett. 415, 90–99. https://doi.org/10.1016/j.epsl.2015.01.037.

Cai, C., Hu, W., Worden, R.H., 2001. Thermochemical sulphate reduction in Cambro–Ordovician carbonates in Central Tarim. Mar. Pet. Geol. 18, 729–741. https://doi.org/10.1016/S0264-8172(01)00028-9.

Cai, C., Li, K., Li, H., Zhang, B., 2008. Evidence for cross formational hot brine flow from integrated 87Sr/86Sr, REE and fluid inclusions of the Ordovician veins in Central Tarim, China. Appl. Geochem. 23, 2226–2235. https://doi.org/10.1016/j.apgeochem.2008.03.009.

Cai, C., Zhang, C., Cai, L., Wu, G., Jiang, L., Xu, Z., Li, K., Ma, A., Chen, L., 2009a. Origins of Palaeozoic oils in the Tarim Basin: evidence from sulfur isotopes and biomarkers. Chem. Geol. 268, 197–210. https://doi.org/10.1016/j.chemgeo.2009.08.012.

Cai, C., Li, K., Ma, A., Zhang, C., Worden, R.H., Xu, Z., Wu, G., Zhang, B., Chen, L., 2009b. Distinguishing the Cambrian source rock from the Upper Ordovician: evidence from sulfur isotopes and biomarkers in the Tarim Basin. Org. Geochem. 40, 755–768. https://doi.org/10.1016/j.orggeochem.2009.04.008.

Cai, C., Zhang, C., Worden, R.H., Wang, T., Li, H., Jiang, L., Huang, S., Zhang, B., 2015. Application of sulfur and carbon isotopes to oil–source rock correlation: a case study from the Tazhong area, Tarim Basin, China. Org. Geochem. 83–84, 140–152. https://doi.org/10.1016/j.orggeochem.2015.03.012.

Cai, C., Xiao, Q., Fang, C., Wang, T., He, W., Li, H., 2016. The effect of thermochemical sulfate reduction on formation and isomerization of thiadiamondoids and diamondoids in the Lower Paleozoic petroleum pools of the Tarim Basin, NW China. Org. Geochem. 101, 49–62. https://doi.org/10.1016/j.orggeochem.2016.08.006.

Cai, C., Li, H., Li, K., Wang, D., 2022. Thermochemical sulfate reduction in sedimentary basins and beyond: A review. Chem. Geol. 607, 121018. https://doi.org/10.1016/j.chemgeo.2022.121018.

Cartwright, J., Huuse, M., Aplin, A., 2007. Seal bypass systems. AAPG Bulletin 91 (8), 1141–1166. https://doi.org/10.1306/04090705181.

Cashman, K.V., Sparks, R.S.J., Blundy, J.D., 2017. Vertically extensive and unstable magmatic systems: A unified view of igneous processes. Science 355, 3055. https://doi.org/10.1126/science.aag3055.

Chen, J., Fu, J., Sheng, G., Liu, D., Zhang, J., 1996. Diamondoid hydrocarbon ratios: novel maturity indices for highly mature crude oil. Org. Geochem. 25, 179–190. https://doi.org/10.1016/S0146-6380(96)00125-8.

Chen, J., Xu, Y., 2019. Establishing the link between Permian volcanism and biodiversity changes: Insights from geochemical proxies. Gondwana Res. 75, 68–96. https://doi.org/10.1016/j.gr.2019.04.008.

Cheng, Z., Zhang, Z., Xie, Q., Hou, T., Ke, S., 2019. Subducted slab-plume interaction traced by magnesium isotopes in the northern margin of the Tarim Large Igneous Province. Earth Planet. Sci. Lett. 489, 100–110. https://doi.org/10.1016/j.epsl.2018.02.039.

Cheng, X., Wu, H.X., Sun, D., Huang, W., Chen, H., Lin, X., Zhu, K., Zhang, F., 2022. The Permian mafic intrusive events in the northwestern margin of the Tarim Basin and their tectonic significance. Acta Petrologica Sinica 38 (3), 743–764. https://doi.org/10.18654/1000-0569/2022.03.09 (in Chinese with English abstract).

Chukwuma, K., Tsikos, H., Horsfield, B., Schulz, H.M., Harris, N.B., Frazenburg, M., 2023. The effects of Jurassic igneous intrusions on the generation and retention of gas shale in the Lower Permian source-reservoir shales of Karoo Basin, South Africa. Int. J. Coal Geol. 269, 104219. https://doi.org/10.1016/j.coal.2023.104219.

Coffin, M.F., Eldholm, O., 1994. Large igneous provinces-crustal structure dimensions, and external consequences. Rev. Geophys. 32 (1), 1–36. https://doi.org/10.1029/93RG02508.

Davies, G.R., Smith, L.B., 2006. Structurally controlled hydrothermal dolomite reservoir facies: an overview. AAPG Bull 90 (11), 1641–1690. https://doi.org/10.1306/05220605164.

Dong, S., Chen, D., Qing, H., Zhou, X., Wang, D., Guo, Z., Jiang, M., Qian, Y., 2013. Hydrothermal alteration of dolostones in the Lower Ordovician, Tarim Basin, NW China: Multiple constraints from petrology, isotope geochemistry and fluid inclusion microthermometry. Mar. Pet. Geol. 46, 270–286. https://doi.org/10.1016/j.marpetgeo.2013.06.013.

Dong, S., Chen, D., Zhou, X., Qian, Y., Tian, M., Qing, H., 2017. Tectonically driven dolomitization of Cambrian to Lower Ordovician carbonates of the Quruqtagh area, north-eastern flank of Tarim Basin, north-west China. Sedimentology 64, 1079–1106. https://doi.org/10.1111/sed.12341.

Duffy, M., Farrell, N., Raeside, R., Muirhead, D., Healy, D., Brasier, A., Schofield, N., 2021. Observations of reservoir quality alteration in proximity to igneous intrusions for two distinct sandstones in Scotland. Mar. Pet. Geol. 129, 105071. https://doi.org/10.1016/j.marpetgeo.2021.105071.

Feng, Z., Hao, F., Tian, J., Zhou, S., Dong, D., Huang, S., 2022. Shale gas geochemistry in the Sichuan Basin, China. Earth-Sci. Rev. 232, 104141. https://doi.org/10.1016/j.earscirev.2022.104141.

Fox, C.P., Whiteside, J.H., Olsen, P.E., Grice, K., 2022. Flame out! End-Triassic mass extinction polycyclic aromatic hydrocarbons reflect more than just fire. Earth Planet. Sci. Lett. 584, 117418. https://doi.org/10.1016/j.epsl.2022.117418.

Frolov, S.V., Akhmanov, G.G., Bakay, E.A., Lubnina, N.V., Korobova, N.I., Karnyushina, E.E., Kozlova, E.V., 2015. Meso-Neoproterozoic petroleum systems of the Eastern Siberian sedimentary basins. Precambrian Res. 259, 95–113. https://doi.org/10.1016/j.precamres.2014.11.018.

He, J., Ding, W., Huang, W., Cao, Z., Chen, E.n., Dai, P., Zhang, Y., 2019. Petrological, geochemical, and hydrothermal characteristics of Ordovician cherts in the southeastern Tarim Basin, NW China, and constraints on the origin of cherts and Permian tectonic evolution. J. Asian Earth Sci. 170, 294–315. https://doi.org/10.1016/j.jseaes.2018.10.030.

Hitzman, M.W., Oreskes, N., Einaudi, M.T., 1992. Geological characteristics and tectonic setting of Proterozoic iron oxides (Cu–U–Au–REE) deposits. Precambrian Res. 58, 241–287. https://doi.org/10.1016/0301-9268(92)90121-4.

Hudspith, V., Scott, A.C., Collinson, M.E., Pronina, N., Beeley, T., 2012. Evaluating the extent to which wildfire history can be interpreted from inertinite distribution in coal pillars: an example from the late Permian, Kuznetsk Basin, Russia. Int. J. Coal Geol. 89, 13–25. https://doi.org/10.1016/j.coal.2011.07.009.

Jacob, H., 1989. Classification, structure, genesis and practical importance of natural solid oil bitumen. Int. J. Coal Geol. 11, 65–79. https://doi.org/10.1016/0166-5162(89)90113-4.

Jiao, S., Zhang, H., Cai, Y., Chen, J., Feng, Z., Shen, S., 2023. Collapse of tropical rainforest ecosystems caused by high-temperature wildfires during the end-Permian mass extinction. Earth Planet. Sci. Lett. 614, 118193. https://doi.org/10.1016/j.epsl.2023.118193.

Karp, A.T., Holman, A.I., Hopper, P., Grice, K., Freeman, K.H., 2020. Fire distinguishers: refined interpretations of polycyclic aromatic hydrocarbons for paleo-applications. Geochim. Cosmochim. Acta 289, 93–113. https://doi.org/10.1016/j.gca.2020.08.024.

Knoll, A.H., Bambach, R.K., Canfield, D.E., Grotzinger, J.P., 1996. Comparative earth history and Late Permian mass extinction. Science 273 (5274), 452–457. https://doi.org/10.1126/science.273.5274.452.

Langhorne, B.S., 2006. Origin and reservoir characteristics of Upper Ordovician Trenton–Black River hydrothermal dolomite reservoirs in New York. AAPG Bulletin 90 (11), 1691–1718. https://doi.org/10.1306/04260605078.

Li, K., Cai, C., Tan, X., Jiang, H., Fan, J., 2022. Multiple fluid flow events and diversity of hydrothermal minerals in Neoproterozoic to lower Paleozoic carbonate reservoirs, Tarim Basin, NW China. J. Asian Earth Sci. 233, 105260. https://doi.org/10.1016/j.jseaes.2022.105260.

Li, H., Lü, T., Pu, H., 2017. LA-ICP-MS zircon U-Pb age of dykes from central Tarim Basin and its geological significance. Geological Bulletin of China 36 (6), 1010–1021 (in Chinese with English abstract).

Li, H., Gao, J., Cao, Z., Zhu, X., Guo, X., Zeng, S., 2023. Spatial-temporal distribution of fluid activities and its significance for hydrocarbon accumulation in the strike-slip fault zones, Shuntuoguole low-uplift, Tarim Basin. Earth Sci. Front. 30 (6), 316–328. https://doi.org/10.13745/j.esf.sf.2023.2.36 (in Chinese with English abstract).

Li, Z., Powell, C.M., 2001. An outline of the palaeogeographic evolution of the Australasian region since the beginning of the Neoproterozoic. Earth-Sci. Rev. 53, 237–277. https://doi.org/10.1016/S0012-8252(00)00021-0.

Li, Y., Su, W., Kong, P., Qian, Y., Zhang, K., Zhang, M., Chen, Y., Cai, X., You, D., 2007. Zircon U–Pb ages of the Early Permian magmatic rocks in the Tazhong–Bachu region, Tarim Basin by LA–ICP–MS. Acta Petrologica Sinica 23 (5), 1097–1107. https://doi.org/10.3969/j.issn.1000-0569.2007.05.022 (in Chinese with English abstract)..

Liu, H., Xu, Y., Zhong, Y., Luo, Z., Mundil, R., Riley, T.R., Zhang, L., Xie, W., 2019. Crustal melting above a mantle plume: Insights from the Permian Tarim Large Igneous Province, NW China. Lithos 326–327, 370–383. https://doi.org/10.1016/j.lithos.2018.12.031.

Lovelock, J.E., Zlatkis, A., Becker, R.S., 1962. Affinity of polycyclic aromatic hydrocarbons for electrons with thermal energies: Its possible significance in carcinogenesis. Nature 193, 540–541. https://doi.org/10.1038/193540a0.

Lu, L., Zhang, Y., Li, Z., Zhang, K., 2023. Petrogenesis of the alkali basalt and trachy-andesite suite in the northern Tarim Basin, NW China: Implications for crust-mantle interactions controlled by the Permian mantle plume. Gondwana Res. 119, 86–103. https://doi.org/10.1016/j.gr.2023.03.010.

McCollom, T.M., Seewald, J.S., Simoneit, B.R.T., 2001. Reactivity of monocyclic aromatic compounds under hydrothermal conditions. Geochim. Cosmochim. Acta 65, 455–468. https://doi.org/10.1016/S0016-7037(00)00533-0.

Monreal, F.R., Villar, H.J., Baudino, R., Delpino, D., Zencich, S., 2009. Modeling an atypical petroleum system: A case study of hydrocarbon generation, migration and accumulation related to igneous intrusions in the Neuquen Basin, Argentina. Mar. Pet. Geol. 26, 590–605.

Morgan, W.J., 1971. Convective plumes in the lower mantle. Nature 230, 42–43. https://doi.org/10.1016/j.marpetgeo.2009.01.005.

Orr, W.L., 1974. Changes in sulfur content and isotopic ratios of sulfur during petroleum maturation—Study of Big Horn Basin Paleozoic oils. AAPG Bulletin 58, 2295–2318. https://doi.org/10.1306/83D91B9B-16C7-11D7-8645000102C1865D.

Othmana, R., Arouri, K.R., Ward, C.R., McKirdy, D.M., 2001. Oil generation by igneous intrusions in the northern Gunnedah Basin, Australia. Org. Geochem. 32, 1219–1232. https://doi.org/10.1016/S0146-6380(01)00089-4.

Palmer, M.R., Elderfield, H., 1985. Sr isotope composition of sea water over the past 75 Myr. Nature 314, 526–528. https://doi.org/10.1038/314526a0.

Peterson, C.H., 2003. Long-term ecosystem response to the Exxon Valdez Oil Spill. Science 302 (5653), 2082–2086. https://doi.org/10.1126/science.1084282.

Pollard, P.J., 2006. An intrusion related origin for Cu–Au mineralization in iron oxide-copper-gold (IOCG) provinces. Mineral. Deposita 41, 179–187. https://doi.org/10.1007/s00126-006-0054-x.

Prasanth, M.P.M., Shellnutt, J.G., Lee, T.Y., 2022. Secular variability of the thermal regimes of continental flood basalts in large igneous provinces since the Late Paleozoic: Implications for the supercontinent cycle. Earth-Sci. Rev. 226, 103928. https://doi.org/10.1016/j.earscirev.2022.103928.

Püttmann, W., Merz, C., Speczik, S., 1989. The secondary oxidation of organic material and its influence on Kupferschiefer mineralization of Southwest Poland. Appl. Geochem. 4, 151–161. https://doi.org/10.1016/0883-2927(89)90046-2.

Qiao, R., Li, M., Zhang, D., Xiao, H., 2024a. Geochemistry and accumulation of the ultra-deep Ordovician oils in the Shunbei oilfield, Tarim Basin: Coupling of reservoir secondary processes and filling events. Mar. Pet. Geol. 167, 106959. https://doi.org/10.1016/j.marpetgeo.2024.106959.

Qiao, R., Li, M., Zhang, D., Xiao, H., 2024b. Distribution and origin of higher diamondoids in the ultra-deep Paleozoic condensates of the Shunbei oilfield in the Tarim Basin, NW China. Org. Geochem. 197, 104883. https://doi.org/10.1016/j.orggeochem.2024.104883.

Richards, M.A., Duncan, R.A., Courtillot, V.E., 1989. Flood basalts and hot-spot tracks: Plume heads and tails. Science 246, 103–107. https://doi.org/10.1126/science.246.4926.103.

Schofield, N., Holford, S., Millett, J., Brown, D., Jolley, D., Passey, S.R., Muirhead, D., Grove, C., Magee, C., Murray, J., Hole, M., 2015. Regional magma plumbing and emplacement mechanisms of the Faroe-Shetland Sill Complex: implications for magma transport and petroleum systems within sedimentary basins. Basin Res. 29 (1), 41–63. https://doi.org/10.1111/bre.12164.

Shellnutt, J.G., Bhat, G.M., Wang, K., Brookfield, M.E., Jahn, B.M., Dostal, J., 2014. Petrogenesis of the flood basalts from the Early Permian Panjal Traps, Kashmir, India: Geochemical evidence for shallow melting of the mantle. Lithos 204, 159–171. https://doi.org/10.1016/j.lithos.2014.01.008.

Shen, A., Hu, A., Cheng, T., Liang, F., Pan, W., Feng, Y., Zhao, J., 2019. Laser ablation in situ U-Pb dating and its application to diagenesis-porosity evolution of carbonate reservoirs. Petroleum Exploration and Development 46 (6), 1127–1140 https://doi.org/10.11698/PED.2019.06.05.

Simoneit, B.R.T., Brenner, S., Peters, K.E., Kaplan, I.R., 1981. Thermal alteration of Cretaceous black shale by diabase intrusions in the Eastern Atlantic—II. Effects on bitumen and kerogen. Geochim. Cosmochim. Acta 45 (9), 1581–1602. https://doi.org/10.1016/0016-7037(81)90287-8.

Simoneit, B.R.T., Fetzer, J.C., 1996. High molecular weight polycyclic aromatic hydrocarbons in hydrothermal petroleums from the Gulf of California and Northeast Pacific Ocean. Org. Geochem. 24, 1065–1077. https://doi.org/10.1016/S0146-6380(96)00081-2.

Sobolev, S.V., Sobolev, A.V., Kuzmin, D.V., Krivolutskaya, N.A., Petrunin, A.G., Arndt, N.T., Radko, V.A., Vasiliev, Y.R., 2011. Linking mantle plumes, large igneous provinces and environmental catastrophes. Nature 477, 312–316. https://doi.org/10.1038/nature10385.

Spacapana, J.B., Palmab, J.O., Gallandc, O., Mancedad, R., Rochae, E., D'Odoricoe, A., Leanzaf, H.A., 2018. Thermal impact of igneous sill-complexes on organic-rich formations and implications for petroleum systems: A case study in the northern Neuquén Basin, Argentina. Mar. Pet. Geol. 91, 519–531. https://doi.org/10.1016/j.marpetgeo.2018.01.018.

Su, A., Wang, Z., Chen, H., Feng, Y., Zhao, J., Jiang, H., Nguyen, A.D., Sun, P., 2024. Temporal constraints on hydrothermal circulation associated with strike-slip faulting in the Permian Maokou carbonates, central Sichuan Basin (SW China). Mar. Pet. Geol. 160, 106643. https://doi.org/10.1016/j.marpetgeo.2023.106643.

Svensen, H., Planke, S., Malthe-Sørenssen, A., 2004. Release of methane from a volcanic basin as a mechanism for initial Eocene global warming. Nature 429, 542–545. https://doi.org/10.1038/nature02566.

Wang, D., Kutuzov, I., Zhang, H., Cao, Z., Wang, Q., Amrani, A., Cai, C., 2024. Application of sulfur isotopes of volatile organic sulfur compounds to determine the natural gas secondary alterations and possible sources in the Tarim Basin, NW China. Mar. Pet. Geol. 169, 107078. https://doi.org/10.1016/j.marpetgeo.2024.107078.

Wang, C., Wu, H., Dilek, Y., Li, Y., Zhang, F., Huang, W., Deng, H., Chen, H., Lin, X., Cheng, X., 2023. Basin filling and magmatic response to the migration of two-stage rifts: New insights into the late Neoproterozoic tectonics of the northern Tarim Craton. Precambrian Res. 397, 107175. https://doi.org/10.1016/j.precamres.2023.107175.

Wiedemeier, D., Brodowski, S., Wiesenberg, G., 2015. Pyrogenic molecular markers: linking PAH with BPCA analysis. Chemosphere 119, 432–437. https://doi.org/10.1016/j.chemosphere.2014.06.046.

Wignall, P.B., 2001. Large igneous provinces and mass extinctions. Earth-Sci. Rev. 53, 1–33. https://doi.org/10.1016/S0012-8252(00)00037-4.

Wu, H., Huang, W., Li, Y., Lin, X., Chen, H., Cheng, X., Zhang, F., 2020. Discovery of Permian mafic sills intrusion event in the Sinian system, Northwest Tarim block. Acta Geologica Sinica 94(6), 1869–1882 (in Chinese with English abstract). https://doi.org/10.3724/SP.J.0001-571720200615.

Wu, L., Jin, Z., Liu, K., Chu, Z., Yang, P., 2021. Evolution of a deeply-buried oil reservoir in the north Shuntuoguole Low Uplift, Tarim Basin, western China: Insights from molecular geochemistry and Re–Os geochronology. Mar. Pet. Geol. 134, 105365. https://doi.org/10.1016/j.marpetgeo.2021.105365.

Xu, H., Liu, Q., Zhu, D., Meng, Q., Jin, Z., Fu, Q., George, S.C., 2021. Hydrothermal catalytic conversion and metastable equilibrium of organic compounds in the Jinding Zn/Pb ore deposit. Geochim. Cosmochim. Acta 307, 133–150. https://doi.org/10.1016/j.gca.2021.05.049.

Xu, H., Liu, Q., Zhu, D., Peng, W., Meng, Q., Wang, J., Shi, J., Jin, Z., 2022. Molecular evidence reveals the presence of hydrothermal effect on ultra-deep-preserved organic compounds. Chem. Geol. 608, 121045. https://doi.org/10.1016/j.chemgeo.2022.121045.

Xu, H., Liu, Q., Jin, Z., Zhu, D., Meng, Q., Wu, X., Li, P., Zhu, B., 2024. Organic compounds in geological hydrothermal systems: A critical review of molecular transformation and distribution. Earth-Sci. Rev. 252, 104757. https://doi.org/10.1016/j.earscirev.2024.104757.

Xu, Y., Wei, X., Luo, Z., Lou, H., Cao, J., 2014. The Early Permian Tarim Large Igneous Province: Main characteristics and a plume incubation model. Lithos 204, 20–35. https://doi.org/10.1016/j.lithos.2014.02.015.

Xu, X., Zuza, A.V., Yin, A., Lin, X., Chen, H., Yang, S., 2020. Permian plume-strengthened Tarim lithosphere controls the Cenozoic deformation pattern of the Himalayan-Tibetan orogen. Geology 49 (1), 96–100. https://doi.org/10.1130/G47961.1.

Yang, J., Cawood, P.A., Montañez, I.P., Condon, D.J., Du, Y., Yan, J., Yan, S., Yuan, D., 2020. Enhanced continental weathering and large igneous province induced climate warming at the Permo-Carboniferous transition. Earth Planet. Sci. Lett. 534, 116074. https://doi.org/10.1016/j.epsl.2020.116074.

Yang, C., Li, M., Ni, Z., Wang, T., Qiu, N., Fang, R., Wen, L., 2022. Paleo-oil reservoir pyrolysis and gas release in the Yangtze Block imply an alternative mechanism for the Late Permian Crisis. Geosci. Front. 13, 101324. https://doi.org/10.1016/j.gsf.2021.101324.

Yunker, M.B., Macdonald, R.W., Vingarzan, R., Mitchell, R.H., Goyette, D., Sylvestre, S., 2002. PAHs in the Fraser River basin: a critical appraisal of PAH ratios as indicators of PAH source and composition. Org. Geochem. 33, 489–515. https://doi.org/10.1016/S0146-6380(02)00002-5.

Zhang, H., Li, Y., Wu, G., Su, W., Qian, Y., Meng, Q., Cai, X., Han, L., Zhao, Y., Liu, Y., 2009. Isotopic geochronology of Permian igneous rocks in the Tarim Basin. Chinese Journal of Geology 44 (1), 137–158 (in Chinese with English abstract). https://doi.org/10.3321/j.issn:0563-5020.2009.01.012.

Zhang, Y., Liu, J., Guo, Z., 2010. Permian basaltic rocks in the Tarim basin, NW China: Implications for plume–lithosphere interaction. Gondwana Res. 18, 596–610. https://doi.org/10.1016/j.gr.2010.03.006.

Zhang, D., Zhang, Z., Santosh, M., Cheng, Z., Kang, J., 2013. Perovskite and baddeleyite from kimberlitic intrusions in the Tarim large igneous province signal the onset of an end-Carboniferous mantle plume. Earth Planet. Sci. Lett. 361, 238–248. https://doi.org/10.1016/j.epsl.2012.10.034.

Zhang, D., Li, M., Qiao, R., Xiao, H., 2024. Applicability and limitation of aromatic maturity parameters in high-maturity oil from ultradeep reservoirs. Energy Fuel. 38 (19), 18413–18430. https://doi.org/10.1021/acs.energyfuels.4c02159.

Zhu, G., Zhang, K., 2022. Did the eruption of the Tarim LIP control the formation of Paleozoic hydrocarbon reservoirs in the Tarim basin, China? Gondwana Res. 101, 224–232. https://doi.org/10.1016/j.gr.2021.08.007.

Zhu, G., Li, T., Zhang, Z., Zhao, K., Zhang, K., Chen, W., Yan, H., Wang, P., 2020. Distribution and geodynamic setting of the Late Neoproterozoic– Early Cambrian hydrocarbon source rocks in the South China and Tarim Blocks. J. Asian Earth Sci. 201, 104504. https://doi.org/10.1016/j.jseaes.2020.104504.